Lab on a Chip

PAPER

View Article Online
View Journal | View Issue

Cite this: *Lab Chip*, 2025, **25**, 5093

Disruption and nebulization of lipid vesicles using surface acoustic waves for direct mass spectrometry

Yuqi Huang,[a] Qian Ma,[b] Ashton Taylor,[b] Lucas Lienard,[c] Theresa Evans-Nguyen [b] and Venkat Bhethanabotla *[a]

Characterizing extracellular vesicles (EVs) using mass spectrometry (MS) provides several advantages. The molecular compositions within EVs can be analyzed at very low concentrations and can also distinguish lipids and molecules with similar structures. However, there are some challenges when analyzing EVs directly using MS, mainly due to their variations in size and biological composition, as well as their tendency to form large clusters. Here, we present a novel surface acoustic wave (SAW) sample preparation system capable of simultaneous disruption and nebulization of liposomes as a model for direct EV analysis by MS. This approach provides a mechanical alternative to traditional chemical methods, which minimizes sample preparation time, volume loss, and chemical interference while enhancing ionization efficiency. We study the influence of frequency on SAW nebulization for MS analysis of DOPC (1,2-dioleoyl-*sn*-*glycero*-3-phosphocholine) liposomes as well as liposome mixture. Through high-frequency Rayleigh SAW excitation, we demonstrate improved liposome disruption and enhanced ionization signals during MS analysis when combined with corona discharge ionization. We systematically investigate key parameters of device frequency, input radio frequency (RF) power, nebulization rate, acoustic heating, aerosolized droplet sizes, and surface preparation. The nebulization process was captured by high-speed imaging, which reveals the critical role of surface treatment and jetting dynamics in achieving efficient nebulization at different frequencies. Our findings reveal the frequency-dependent nature of Rayleigh SAW nebulization, highlighting its ability to generate fine, aerosolized particles that enhance MS sampling reliability and ionization efficiency. This work represents a significant advance in MS sample preparation techniques, with broad implications for lipidomics and growing interest in the analysis of biologically relevant vesicles such as EVs.

Received 13th July 2025,
Accepted 18th August 2025

DOI: 10.1039/d5lc00692a

rsc.li/loc

Introduction

Liposomes are spherical vesicles that contain one or more phospholipid bilayers.[1,2] Due to their ability to carry cargo and flexible size, liposomes are widely used in research and the biomedical field.[2,3] Liposomes comprise a vehicle for drugs because they can incorporate hydrophilic or hydrophobic compounds and deliver the cargo to specific target sites.[4–6] Mass spectrometry (MS) analysis on liposome carriers allows for the exploration of lipid compositions, lipid–lipid and lipid–protein interactions, and quantification of encapsulated substances within liposomes.[7–9]

However, it is challenging to directly analyse lipids because the complex nature of lipid vesicles with polar and non-polar lipids requires different extraction and separation techniques.[10,11] Additionally, disruption of liposome membranes is often necessary to ensure efficient ionization on encapsulated contents suitable for analysis.[12,13] Traditional chemical methods, such as using organic solvents and detergents, can chemically alter vesicle cargo including sensitive biomolecules like proteins, potentially compromising analytical results.[14,15] Another existing challenge is the presence of non-polar lipid composition, such as cholesterol, which can further complicate ionization using conventional MS techniques like electrospray ionization (ESI).[16,17] ESI is vulnerable to fouling during the sampling of lipids.[18] While matrix-assisted laser desorption ionization (MALDI) is another commonly used ionization technique, as is ESI, offers minimal sample preparation, but can suffer from matrix interference with low mass species such as cholesterol.[18,19] Given these challenges, it is

[a] *Department of Chemical, Biological, and Materials Engineering, University of South Florida, Tampa, FL 33620, USA. E-mail: bhethna@usf.edu*
[b] *Department of Chemistry, University of South Florida, Tampa, FL 33620, USA*
[c] *Department of Material Sciences, Polytech Dijon, Dijon, 21000, France*

worthwhile to explore a novel, mechanical sampling approach that preserves the aqueous environment and minimizes interference for lipid and vesicle cargo analysis.

Surface acoustic wave (SAW)-based methods offer a promising solution by providing a mechanical approach to lyse biological vesicles and prepare samples for MS analysis through effective nebulization. SAW devices are capable of generating strong pressure gradients and induce acoustic streaming, which can result in appreciable shear stresses on cells, particularly under high-power operation and in the presence of standing wave field.[20] Acoustic wave devices have a wide range of applications in various fields, including radio frequency filters, biosensors, chemical sensors, cell lysis, particle separation, and microfluidics.[21–28] SAW waves are generated by applying an RF signal to interdigital transducers (IDTs), which convert electrical signals into mechanical waves *via* piezoelectricity. Among various types of SAW propagation modes, Rayleigh waves are confined near the surface of the piezoelectric substrate and its energy dissipates when encountering a liquid droplet, leading to fluidic streaming, acoustothermal heating, and liquid aerosolization.[18,29]

Among available piezoelectric materials for SAW excitations, lithium niobate ($LiNbO_3$) and zinc oxide (ZnO) have been studied for fluid nebulization. ZnO is attractive for circuit integration due to its ease of sputtering onto various substrates.[30] However, its use in high-frequency SAW nebulization requires significantly higher RF power than bulk $LiNbO_3$, which can cause excessive jetting that hinders MS sampling.[30–32] Additionally, ZnO's polycrystalline nature from sputtering deposition results in spurious wave generation that can reduce nebulization efficiency.[32] In contrast, $LiNbO_3$ offers superior performance with a higher electromechanical coupling coefficient and stable single crystal structure, which offers efficient energy transfer and better wave stability.[30] These properties reduce acoustic losses, suppress spurious wave, and enhance nebulization consistency, making $LiNbO_3$ the preferred material for high-frequency SAW-based MS sampling in this work.

A few previous studies have demonstrated the potential of SAW for MS sampling and, separately for biological vesicle lysis. For example, Goodlett *et al.* employed SAW nebulization to MS for the detection of lipids and peptides.[18,33–35] We have previously demonstrated improved ionization efficiency for both polar and non-polar analytes by coupling SAW nebulization with atmospheric-pressure chemical ionization (APCI), where a high voltage (3 kV) is applied to the APCI needle to activate corona discharge (CD) ionization.[36] In another previous publication, we presented the effect of SAW force magnitude in particle manipulation, showing that increasing SAW resonant frequency enhances the radiation pressure forces exerted on smaller particles.[37] Building on these principles and findings, we also recently demonstrated that high-frequency SAWs (10–100 MHz) can mechanically disrupt liposomes without chemical lysing agents. Using a two-stage SAW platform, liposomes were lysed on a high-frequency chip and then transferred to a low-frequency SAW nebulization device. This approach allowed the detection of DOPC (1,2-dioleoyl-*sn-glycero*-3-phosphocholine) liposomes at low concentrations using MS analysis.[23] Despite these advances, the two-chip platform presents several drawbacks, including sample volume loss, potential contamination, and lipid re-aggregation during transfer between devices with separate lysing and nebulization purposes.

To address these limitations, in this work, we develop and present a single-chip SAW platform capable of simultaneous liposome disruption and nebulization. This novel design simplifies the MS sampling process, minimizes sample loss, and enhances automation. In this study, we systematically designed and characterized SAW nebulizers operating at various resonant frequencies to evaluate their effects on liposome disruption, nebulization, and subsequent MS analysis. Parameters such as aerosolized droplet sizes, thermal effects, and nebulization speed were systematically evaluated to understand their frequency-dependent effects on signal intensity for MS analysis. The results demonstrate that this single-chip SAW platform significantly advances sample preparation techniques for lipidomics by providing a novel sampling method for analysing vesicles with improved reliability and ionization efficiency.

Materials and methods

Surface acoustic wave nebulization devices

SAW devices with resonant frequencies from 10 MHz to 50 MHz were designed and fabricated to study the frequency dependence of droplet nebulization and liposome disruption efficiency. Each SAW device features two regions of interdigitated transducers (IDTs), and the sample region is placed on the bare lithium niobate substrate in between the two IDT region electrode. The reflector electrodes that have the spacing and width of a quarter of the wavelength are patterned next to the IDT region, where the wave energy is partially reflected into the sample region to improve energy efficiency. The measurements resonant frequencies from lowest insertion loss of *S*-parameters, device wavelength, IDT apertures, reflector apertures, delay line length, liposome of reflectors and finger pairs are shown in Table 1 and Fig. 1.

The fabrication of SAW devices starts with a cleaned 4 inch, double-side polished 128° YX-cut $LiNbO_3$ substrate (University Wafer, Inc.). The thickness of the wafer chosen is 1 mm because thicker wafers withstand higher power and thermal-related stresses. The substrate was first cleaned with acetone, methanol, and DI-water, then dried with N_2 and placed on an 80 °C hot plate to remove excessive moisture. A 2 μm layer of negative photoresist (NR9-1500py, Futerrex) was spin-coated onto the substrate. After pre-bake at 125 °C for 2 minutes, the photoresist is UV-exposed (Karl Suss MA-56) and followed by a post bake (2 min, 125 °C). The cured photoresist is then developed in resist developer RD6 (Futerrex) for 14 s. The thickness of the developed photoresist pattern was verified at multiple wafer locations using a stylus profiler (Dektak D150) to confirm consistent

Table 1 Design parameters and measured resonant frequencies of SAW devices

Frequency (MHz)	Wavelength (μm)	IDT aperture (mm)	Reflector aperture (mm)	Delay line length (mm)	Reflector #	Finger pair #
9.24	414	10	10.2	6.2	20	20
19.63	200	10	10.2	6.2	30	35
29.49	132	9.4	9.6	5.2	32	60
40.49	96	9.4	9.6	5.2	60	60
49.89	80	9.2	9.4	5	64	64

pattern formation and target thickness. Final pattern quality and completeness were also inspected using an optical microscope (Mitutoyo Corp). Metal deposition of a 10/100 Cr/Au layers using e-beam evaporation (AJA International Inc.) followed at a chamber pressure of 1×10^{-5} Torr. The SAW device is finished by using an acetone lift-off. In order to protect the IDT electrodes as well as the metal traces, the wafer is spin-coated with an 1.4 μm thick epoxy-based negative photoresist (SU-82002, Kayaku Advanced Materials) with similar pre-bake (1 min, 95 °C), UV-exposure, post-bake (2 min, 95 °C), resist development (SU-8 resist developer, Fisher Scientific), and thermal hard cure (10 min, 175 °C). To evaluate the acoustic impact of this SU-8 passivation layer, we measured the S_{21} response before and after coating. The insertion loss increased by ~2.5–3.5 dB after SU-8 deposition (Fig. S5), indicating moderate acoustic attenuation due to the viscoelastic nature of the layer. The SU-8 thickness was minimized (~1.4 μm) to reduce both damping and thermal effects, and it was not applied to the delay line to preserve wave–fluid interaction. For the measurements shown in Fig. 2, S_{21} data were collected using a newly fabricated set of devices mounted on a test fixture positioned directly below the MS, replicating the experimental setup. The test fixture includes a metal probe arm with an SMA-connected interface, and the measurement *S*-parameter files were de-embedded up to the tip of the arm to account for fixture loss. This approach ensured that the S_{21} response reflects the mounted device behaviour under actual operating conditions.

DOPC liposomes and DOPC/DOPE mixture preparation

The DOPC (1,2-dioleoyl-*sn-glycero*-3-phosphocholine) liposomes were prepared using similar methods detailed in our previous research article by Taylor *et al.*[23] Specifically, a 1 mg mL^{-1} DOPC in chloroform solution (Avanti Polar Lipids) was evaporated in a 25 mL round-bottom flask under vacuum. The resulting lipid film is then rehydrated in filtered HPLC water and mixed on the rotary evaporator for 2 hours, and then put into a sonicator bath to form multilamellar vesicles. The vesicle solution was passed through a size extruder 11 times to produce unilamellar liposomes with a diameter of approximately 100 nm, verified by dynamic light scattering (Zetasizer Nano, Malvern Instruments). The liposome stock solution at a concentration of 1 mg mL^{-1} was diluted in ammonium acetate spiked LC/MS grade water (Fisher Scientific). Ammonium acetate can facilitate ionization at lower concentrations. The resulting sample concentration used for MS analysis is 50 μM DOPC in 150 mM ammonium acetate.

Similarly, A lipid mixture of 1,2-dioleoyl-*sn-glycero*-3-phosphocholine (DOPC) and 1,2-dioleoyl-*sn-glycero*-3-phosphoethanolamine (DOPE) was used to prepare vesicles with a 1 : 1 molar ratio. A chloroform solution containing 1 mg mL^{-1} DOPC and 0.95 mg mL^{-1} DOPE (Avanti Polar Lipids) was evaporated to form a thin lipid film, which is then rehydrated with a 150 mM ammonium acetate solution prepared in LC/MS-grade water and agitated on a rotary evaporator for 3 hours. The resulting suspension was sonicated in a bath sonicator for 30 minutes to promote vesicle formation, and then extruded 11 times through 100 nm polycarbonate membranes (Whatman) to obtain uniform unilamellar liposomes (DLS verified size at 100 nm shown in Fig. S7). The final total lipid concentration was 50 μM (25 μM DOPC and 25 μM DOPE).

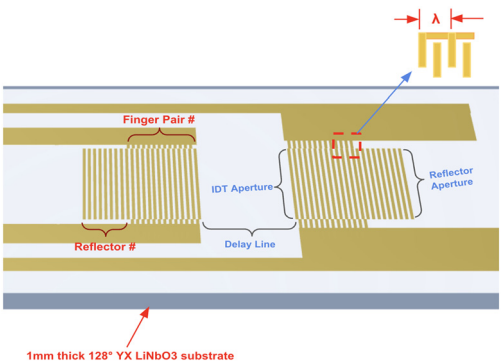

Fig. 1 Schematic illustration of the SAW nebulization device.

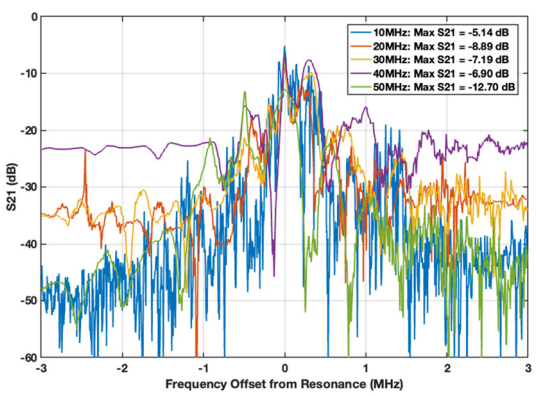

Fig. 2 S_{21} (dB) as a function of normalized frequency offset from resonance.

Sample nebulization test and device setup

To generate Rayleigh waves on the fabricated SAW devices, the resonant frequencies of SAW devices were first identified using a handheld vector network analyzer (AURSINC NanoVNA-H4) at the lowest insertion loss. The exact frequencies for the 10 MHz to 50 MHz devices are recorded in Table 1, The S_{21} responses with respect to devices resonant frequencies are recorded in Fig. 2. It is observed that all measured resonant frequencies are slightly lower than the theoretical values, which are determined by the ratio of Rayleigh wave propagation speed (3960 m s^{-1}) to the designed IDT wavelength (Table 1, column). This discrepancy is mainly due to the actual SAW velocity being reduced from the mass loading effects of the high-density gold electrode as well as the SU-8 photoresist layer deposited on top of the IDT. An RF signal generator (DSG815, Rigol) was connected to an RF amplifier (ZHL-100 W-GAN+, Mini-Circuits) and then to a high-power RF splitter to provide both IDT regions with RF power at their resonances.

To further study and characterize the nebulization behaviour under different conditions, the nebulization process was recorded using a high-speed video camera (Phantom VEO640S) at a frame rate of 3000 frames per second. Water droplets with a volume of 1 μL were placed on 30 MHz SAW devices for high-speed camera imaging. One device was treated with oxygen plasma (Harrick Plasma) at 500 mTorr for 2 minutes to enhance surface wettability, while another 30 MHz device remained untreated. Droplet aerosol size distributions at different resonant frequencies were measured using an optical particle sizer (OPS 3330, TSI). Temperature changes during SAW nebulization were monitored using an infrared thermal camera (FLIR T420).

Ionization methods and mass spectrometry experiment

The 1,2 dioleoyl-*sn-glycero*-3-phosphocholine (DOPC) liposomes with an average diameter of 100 nm were diluted in 150 mM ammonium acetate LC/MS-grade water to achieve a final lipid concentration of 50 μM. The MS analysis on liposomes sample was performed on an ion trap mass spectrometer (LTQ XL, Thermo Scientific). In-source fragmentation at 50 V was used to break apart adducts and improve signal quality. The fabricated SAW device was positioned 5 mm underneath the inlet ion transfer tube. An APCI needle (PS350, Stanford Research System) was placed above the liposome sample, and 5 mm away from the ion transfer tube. The voltage supplied to the needle was set to +3.4 kV to apply a corona discharge to the nebulized liposome sample aerosol for sample ionization. Mass spectrometry data, as well as the extracted ion chromatogram (EIC) for DOPC over the sample volume, were collected from each run to study the frequency-dependent disruption efficiencies during sample nebulization (Fig. 3). Since the hydrophilic effect from O_2 plasma treatment is known to degrade over time, plasma treatment was reapplied after approximately every 30 experimental trials, or earlier if sample spreading or nebulization behaviour became inconsistent. This protocol ensured stable droplet contact and reproducible nebulization across all experiments.

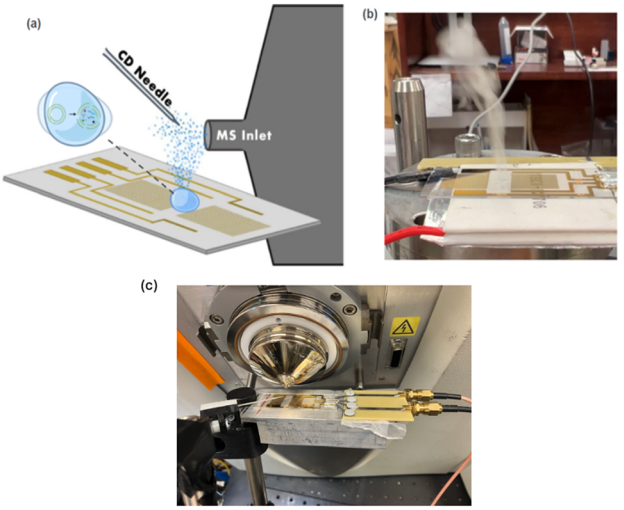

Fig. 3 (a) Schematic diagram of SAW disruption and nebulization with APCI needle and MS; (b) SAW nebulization in action; (c) SAW nebulization with APCI needle for MS sampling.

Results and discussion

Droplet nebulization experiments

When RF power is applied at the device's resonant frequency, a surface acoustic wave (SAW) is generated and propagates along the substrate surface. As the wave reaches a liquid droplet, a portion of its energy couples into the fluid *via* the Rayleigh wave's longitudinal component, resulting in a leaky SAW that penetrates the liquid and induces internal streaming. This coupling occurs at the Rayleigh angle.[38,39] The refracted acoustic waves in the droplet generate internal streaming capillary waves, and jet formation or atomization at sufficiently high power.[40] Liquid jetting typically involves the ejection of high-velocity, narrow streams that can produce smaller droplets through fragmentation, whereas atomization refers to the broader breakup of the fluid into a fine mist *via* film rupture or capillary wave instabilities.[41] Collins *et al.* studied that the interaction of the SAW with the liquid dynamically alters its wetting properties, leading to a significant reduction of the three-phase contact angle at the front of the thin liquid film.[45]

This quasi-steady liquid film is sometimes referred to acoustowetting and is crucial for nebulization to occur.[42,43,45]

Examples of nebulization behaviour from 1 μL droplets are captured *via* high-speed camera imaging Fig. 4 and 5. A 30 MHz device is operated at 7 watts on a delay line with and without oxygen plasma treatment (Fig. 4 and 5). When RF power is applied to the 30 MHz SAW device, Rayleigh waves

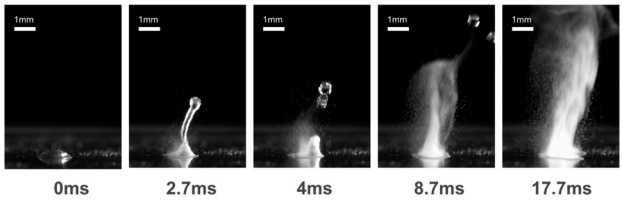

Fig. 4 High-speed frames of a 1 μL droplet on a 30 MHz SAW device without O_2 plasma treatment recorded at 0 ms, 2.7 ms, 4.0 ms, 8.7 ms, and 17.7 ms after SAW activation. In the untreated case, SAW actuation quickly induces a strong ejection of several large satellite droplets in narrow jets (2.7–8.7 ms). These satellites are expelled at high velocity.

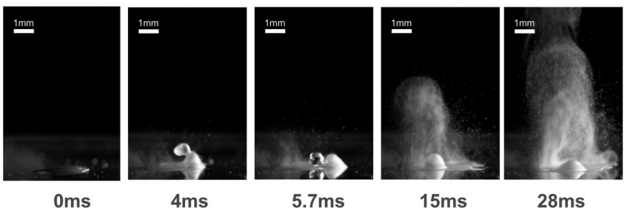

Fig. 5 High-speed frames of a 1 μL droplet on a 30 MHz SAW device with O_2 plasma treatment, recorded at 0 ms, 4.0 ms, 5.7 ms, 15 ms, and 28 ms after SAW activation. In sharp contrast, the plasma-treated surface. The fluid is held in place which allows a larger sample volume to be sent to the MS compared to the untreaded group.

propagate along the $LiNbO_3$ substrate and couple into the droplet. From timepoints across both nebulization modalities, several stages can be clearly identified. Fig. 4 and 5 shows the formation of capillary wave and satellite droplet pinch-off on the droplet surface at the onset of SAW activation (within 5 ms). For the untreated 30 MHz device, the formation of large-jetted satellite droplets from the primary droplet are ejected vertically outside the capturing frame. The measurements of the jetted particles estimate diameters of about 400–700 microns. At higher frequencies, the capillary waves on the droplet's surface become more pronounced, and jetted volume from the primary droplet before nebulization has increased significantly. Overall, the oxygen plasma induced wettability dramatically improves SAW nebulization by anchoring the droplet and ensuring a uniform thin film, which minimize erratic jetting and produce a smooth continuous aerosol plume, ensuring consistent sample delivery into the MS.

During MS sampling, occasionally, undesirable sample traveling is associated with the coupled-resonator design of the SAW devices, primarily due to the slight resonance variations attributable to the fabrication process. Such differences can cause the input frequency (measured from the S_{21} parameter) to align more closely with one port than the other, leading to an imbalance in the amplitude of the standing wave forces. The minimum input RF power to initiate nebulization, as well as the maximum droplet volumes associated with those input powers for every device frequency is presented in Table 2. Note that all devices were oxygen plasma treated.

Table 2 Input RF power and maximum droplet volume for initiating stable nebulization across devices. Input powers were minimized at each frequency to enable sustained nebulization while limiting heating and avoiding jetting artifacts, in line with practical MS integration needs

Device frequency (MHz)	Minimum power (Watt, estimated)	Maximum sample allowed (μL)
10	2	>5
20	3	>5
30	5	~1
40	7	0.5
50	13.97	0.3

The averaged nebulization rate *versus* input RF power is presented in Fig. 6. The rate is calculated from the ratio of nebulized droplet volume to the time taken for sample to disappear completely. The added volume droplets for 10 to 50 MHz devices are 5 μL, 5 μL, 0.5 μL, 0.5 μL, 0.3 μL. It is observed that the nebulization rate is increased with larger input RF power, as well as decreased droplet volume. This observation is consistent with the ZnO/Si SAW nebulization device reported by Guo *et al.*[32] We found that maintaining a steady, moderately low nebulization rate during MS sampling can minimize sample loss caused by the limited suction capacity of the ion transfer tube. Additionally, it improves ionization efficiency by preventing excessive moisture accumulation on the corona discharge needle, thereby enhancing the consistency and reliability of the results.

Frequency dependent droplet size characterization

Fig. 7 presents the mean size distributions of aerosolized droplets generated by SAW nebulization at resonant frequencies ranging from 10 MHz to 50 MHz. Measurements were obtained using an optical particle sizer capable of detecting particles between 300 nm and 10 μm, segmented into 16 user-adjustable bins. The raw data corresponding to the size distributions at each frequency (shown in Fig. S6) are available in the SI. At lower frequencies nebulizations, particularly 10 MHz and 20 MHz, particle counts reached or

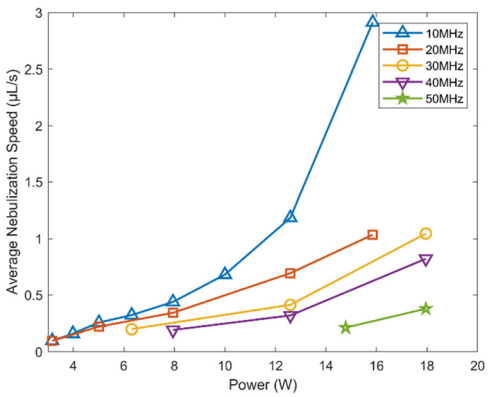

Fig. 6 Average nebulization rate (in μL s^{-1}) *versus* input RF power for every frequency.

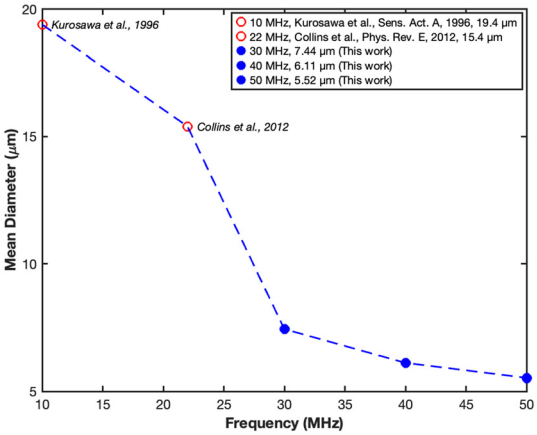

Fig. 7 Mean droplet diameter as a function of SAW excitation frequency. Blue data points represent measurements from the particle sizer. Red points indicate literature-reported values from Kurosawa *et al.* (1996)[44] at 10 MHz and Collins *et al.* (2012)[45] at 22 MHz. The observed inverse relationship between frequency and droplet size is consistent with capillary wave scaling theory, supporting the use of higher-frequency SAWs for generating smaller droplets in nebulization applications.

exceeded the sizer's upper limit, indicating the mean droplet sizes above 10 μm. For these lower frequencies (10 MHz and 22 MHz), data were extracted from previously published studies. Specifically, Kurosawa *et al.* reported a mean droplet diameter of approximately 19 μm at 10 MHz.[44] Collins *et al.* (2012) reported two mass median droplet peaks at 1.21 μm and 15.4 μm under 22 MHz excitation, with the dominant larger mode at 15.4 μm corresponding to atomization from the thin-film region.[45] In contrast, the mean droplet sizes measured in this work for higher frequencies were in smaller sizes: 7.44 μm at 30 MHz, 6.11 μm at 40 MHz, and 5.52 μm at 50 MHz.

This trend is consistent with the physical model proposed by Collins *et al.*,[45] in which atomization from SAW-induced thin films is governed by acoustic streaming and radiation pressure that modify the film's geometry. Specifically, SAWs diffract into the liquid at the Rayleigh angle, generating both acoustic radiation pressure and boundary-layer streaming flows that redistribute fluid into a thin, quasi-steady film. The geometry of this film is characterized by its height H and length L, which can determine the dominant instability wavelength λ that sets the droplet diameter. Experiments revealed that diameter scales inversely with operating frequency under a balance of capillary and viscous stresses. Thus, the observed decrease in droplet size with increasing SAW frequency is attributed to shorter acoustic wavelengths, which lead to thinner and shorter films and in result of finer droplets. Notably, this mechanism is facilitated by O_2 plasma treatment of the substrate, which reduces the contact angle and promotes enhanced wettability. A more wettable surface allows for the formation of thinner, more stable films with larger lateral spread, improving the coupling of acoustic energy into the fluid and suppressing premature jetting or dewetting. This results in a more uniform atomization front and supports efficient breakup into smaller droplets.

In addition to the observed frequency-dependent trends, recent studies suggest that classical capillary wave models alone are insufficient to fully explain the mechanisms of SAW-driven nebulization.[46] While Kelvin's equation can predict a scaling relationship between frequency and droplet size *via* capillary wave breakup, emerging experimental and theoretical insights reveal that multiple droplet generation mechanisms act in parallel within a SAWN system. Research shows that SAW nebulization involves multiple droplet-generation mechanisms acting simultaneously. Jetting and whipping phenomena arise when high local acoustic pressures deform the liquid into crests or ridges, which then pinch off into larger, irregular droplets,[47] which agrees with the observation from the high-speed camera in this work. At higher acoustic intensities or with thicker films, cavitation becomes significant and leads to vapor bubbles formation and collapse, which launches high-velocity micro-jets that eject smaller droplets.[46,48] In parallel, large oscillating liquid domes or films may fragment due to instability and produce both fine and coarse droplets, resulting in multimodal droplet size distributions.[49,50]

Acoustothermal effect

SAWs notably produce heating effects both in the piezoelectric substrate and liquid sample as the wave propagates through these media. Acoustic heating within the device substrate can be attributed to several mechanisms, including ohmic losses in the metallic bus bars and metal traces,[51] as well as thermoelastic damping where heat is produced from oscillating deformation (mechanical waves) within the piezoelectric material, causing internal friction between molecules. On the other hand, when SAWs interact with a liquid droplet, acoustic energy is imparted into the liquid, triggering droplet actuation, acoustic streaming, and atomization. The absorption of acoustic energy through viscous damping—where both shear and bulk viscosities play critical roles—leads to a temperature rise within the fluid layer.[52–54]

While SAW devices are widely used in biosensing and biological sample manipulation, one needs to take extra precautions when working with temperature-sensitive biomolecules. Excessive or unstable heating during SAW operations may cause analyte degradation, leading to compromised data consistency and reliability. Therefore, maintaining an optimized thermal range is important to preserve sample integrity and ensure accurate results. To study the acoustic heating effect from SAW, we measured the surface temperature of a 0.5 μL water droplet on the delay line using an infrared camera. The recorded duration of nebulization is controlled within 3 seconds to match the actual MS sampling time, and the maximum temperature of the droplet sampling region was recorded at different SAW

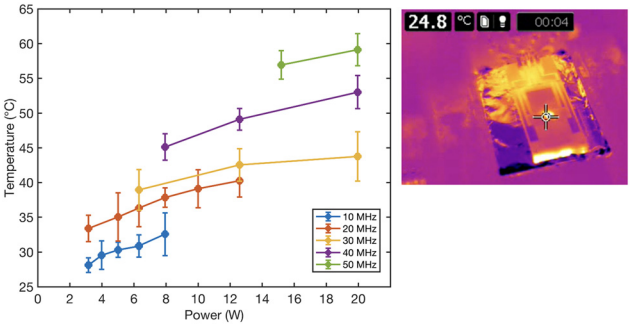

Fig. 8 Maximum temperature of droplet nebulization at different input powers and nebulization frequencies.

nebulization frequencies and RF powers, with results shown in Fig. 8. Across all frequencies, the average temperature rises as excitation power increases. This thermal effect is amplified at higher frequency, for example, at 8 W, 40 MHz shows a much higher temperature increase compared to 10 MHz. This enhanced thermal response may be attributed to more efficient energy transfer at elevated excitation powers and frequencies. We note that both the $LiNbO_3$ substrate and water droplets used in our measurements are non-blackbody emitters which may introduce some underestimation in absolute temperature values. To account for this, all measurements were performed under consistent viewing angles and environmental conditions, and the results are interpreted primarily in a relative manner to compare thermal trends across frequencies and power levels. The goal of this analysis is not to report exact surface temperatures, but to illustrate the relative magnitude of acoustothermal heating and its correlation with SAW frequency and input power.

It is worth noting that under high RF power, the $LiNbO_3$ substrate can be subjected to breaking due to several intrinsic material responses, including mechanical deformation when exposed to electric fields, as well as sharp thermal gradients and resulting in stress from uneven expansion. Thermal failure is also a major factor to wafer breakage during device fabrication, where the temperature needs to be slowly increased with an anti-static blower to keep removing static charges built up during heating. Developing a robust device capable of withstanding high power while minimizing heat transfer to the sample requires careful consideration of multiple design factors and system configurations. Several strategies can be considered to enhance device durability, including using a thicker substrate, incorporating a metallic holder with an integrated heat sink, cooling the device with a Peltier cooler, configuring the RF generator to operate at a reduced duty cycle, as well as optimizing the metal trace and SAW design on the substrate to enhance energy efficiency and SAW stability. These modifications can all be considered to contribute to improving thermal management and device ruggedness under high-power conditions.

Frequency-dependent SAW disruption/nebulization of liposomes

To demonstrate the effects of different SAW frequencies on liposome sample disruption and nebulization, we performed MS analysis of 0.3 μL of 50 μM DOPC (15 pmol total) in 150 mM ammonium acetate nebulized resonant frequencies of 10, 20, 30, 40, and 50 MHz. A fixed sample volume of 0.3 μL was used across all conditions to eliminate variability from droplet volume. The RF power was individually adjusted to the minimum level required for stable nebulization at each frequency, ensuring a consistent nebulization rate and effective aerosol intake through the orifice.

Fig. 9 presents representative mass spectra collected from 10 MHz to 50 MHz. Across all conditions, several primary peaks were consistently observed, including the phosphocholine fragment $[PC]^+$ at 184.1 *m*/*z*, the protonated DOPC monomer $[DOPC + H]^+$ at 786.5 *m*/*z*, and the DOPC dimer $[2DOPC + H]^+$ at 1571.8 *m*/*z*. Additional low-abundance adduct ions were detected, including oxygen adducts (*e.g.*, +O to +6O) from 802.5 to 882.5 *m*/*z* and sodium adducts at 808.5 *m*/*z*.

Fig. 10 shows the extracted ion chromatogram (EIC) results, calculated as the summed peak areas of the DOPC monomer and dimer across the entire signal duration (<3 s).

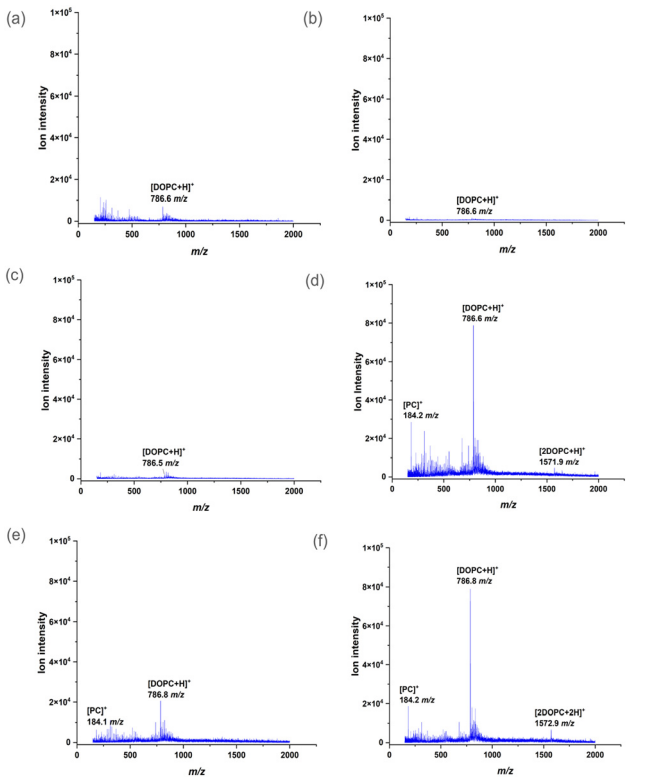

Fig. 9 Mass spectra of DOPC obtained under different excitation conditions: (a) 10 MHz at room temperature, (b) 10 MHz with 60 °C sample, (c) 20 MHz, (d) 30 MHz, (e) 40 MHz, and (f) 50 MHz. All spectra show a prominent peak corresponding to the protonated DOPC monomer ($[DOPC + H]^+$, ~786.6 *m*/*z*).

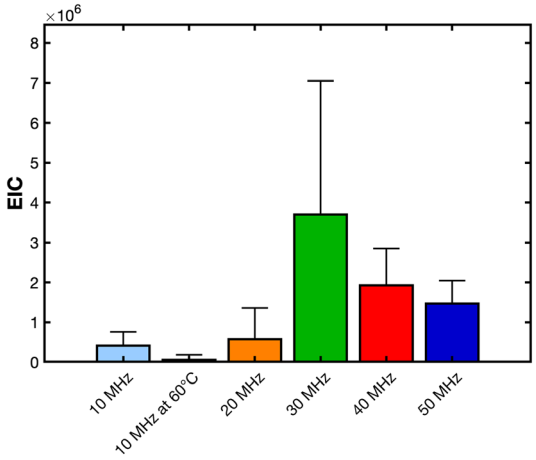

Fig. 10 Extracted ion chromatogram (EIC) signal intensities for DOPC at varying SAW frequencies. Data include excitation at 10 MHz, 10 MHz with elevated temperature (60 °C), and higher frequencies up to 50 MHz. Increased EIC at 30–50 MHz indicates more efficient lipid nebulization at higher acoustic frequencies.

Notably, the highest ion signal was observed at 30 MHz (~3.7 × 10^6), followed by 40 MHz (~1.93 × 10^6) and 50 MHz (~1.47 × 10^6). These were significantly higher than signals obtained at 10 MHz (~4.1 × 10^5) and 20 MHz (~5.75 × 10^5). To evaluate whether this enhancement resulted from temperature alone, we conducted a control test at 10 MHz after preheating the DOPC sample in a 60 °C water bath for 3 minutes. This condition produced a reduced signal (~5.87 × 10^4), indicating that heating alone can reduce ionization efficiency. These findings suggest that the improved ion signals at higher frequencies stem primarily from enhanced SAW-driven vesicle disruption and finer droplet atomization, rather than temperature effects. Higher frequencies generate smaller aerosol droplets with greater surface-to-volume ratios, promoting more efficient ionization by the APCI needle.

In contrast, the 10 MHz trials showed considerable variability. Usable DOPC signals were recovered in fewer than half of the repeated trials, while the remaining attempts yielded no detectable ion peaks. In one instance, operation at 10 MHz triggered a vacuum level error from the MS turbo pump, necessitating equipment cleaning and recalibration. This performance inconsistency is likely due to insufficient vesicle disruption and the formation of larger aerosol droplets, which are less efficiently ionized and may clog the MS inlet. Larger droplets at low frequencies can also accumulate on the APCI needle, leading to short circuits and diminished ionization efficiency. No such signal dropout or equipment issues were observed in the 30–50 MHz trials, all of which consistently produced DOPC ion peaks over five consecutive runs. The improved reproducibility and signal strength at these higher frequencies underscore the value of frequency-optimized SAW nebulization.

For general application, it is critical to calibrate droplet volume for each frequency to avoid sample jetting, especially at high power levels. Variations in solvent viscosity, density, and contact angle can lead to satellite droplet formation, which may contaminate the APCI needle or ion transfer tube. Such fouling can short-circuit the needle or cause clogging, increasing background noise and requiring frequent maintenance. These complications were most apparent in the 10 MHz and 20 MHz groups and were largely absent in the higher-frequency devices.

SAW nebulization of mixed-lipid vesicles

To evaluate the generality of our SAW nebulization platform, we performed additional experiments using liposomes composed of a binary DOPC/DOPE mixture (1 : 1 molar ratio, 50 μM total lipid concentration). These vesicles were nebulized directly from 0.3 μL droplets at resonant frequencies of 10 MHz and 50 MHz under conditions identical to those used for pure DOPC. Mass spectrometry analysis revealed strong and reproducible signals for both DOPC ($[M + H]^+$, 786.6 *m*/*z*) and DOPE ($[M + H]^+$, 744.5 *m*/*z*) as well as their corresponding dimers, under 50 MHz nebulization. In contrast, nebulization at 10 MHz yielded significantly weaker signals, and in 3 of the 7 trials, no discernible peaks were detected. We have also noticed the damaged toward the pumping system causing the mass spectrometer to shut down after 10 trials at 10 MHz. Fig. 11(b) and (c) show representative spectra from the 10 MHz and 50 MHz conditions, respectively.

Extracted ion chromatogram (EIC) data from 10 MHz and 50 MHz nebulization are summarized in Fig. 11(c). The 50 MHz device achieved an average total EIC peak area of 5.65 × 10^6 compared to 1.60 × 10^6 for 10 MHz. These findings support the frequency-dependent enhancement of ionization

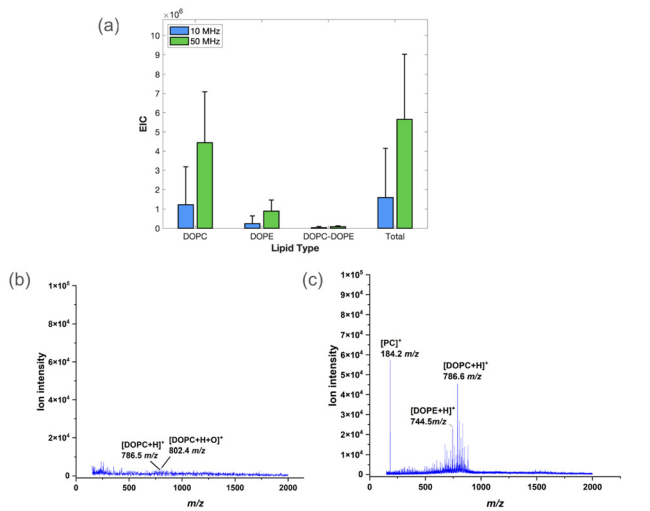

Fig. 11 (a) Recovered EIC signals for individual lipid species and total signal at 10 MHz and 50 MHz. Quantified species include DOPC, DOPE, the heterodimer DOPC–DOPE, and the total recovered signal intensity. (b) and (c) Representative mass spectra showing ion intensity *vs.* *m*/*z* at 10 MHz and 50 MHz excitation, respectively. Enhanced signal intensity at 50 MHz reflects improved nebulization and lipid release efficiency.

efficiency and extending the utility of the SAW nebulization platform to mixed-lipid vesicles and reinforcing its relevance for analysing biologically representative systems such as extracellular vesicles.

Conclusions

In this study, we demonstrated that higher frequency surface acoustic wave devices provide a simple yet powerful method for the direct mass spectrometry (MS) analysis of liposomes. Compared with traditional chemical-based disruption techniques, SAW enables efficient mechanical disruption and nebulization of DOPC liposomes samples, addressing key limitations such as chemical interference and extensive preparation times. At higher frequency nebulization the ion signals are significantly enhanced, and the extracted ion chromatograms reveal a clear frequency-dependent trend. This improvement is achieved despite the reduced sample volume required to mitigate liquid jetting at higher frequencies. The enhanced ionization efficiency is attributed to the combination effects of mechanical disruption of liposome vesicles by SAW and the generation of finer aerosolized droplets with an increased surface area-to-volume ratio, which facilitates more effective ionization by the high-voltage APCI needle.

These results highlight the potential of high-frequency SAW devices as an effective and innovative alternative to conventional MS sampling techniques. The single-chip SAW platform offers a simplified and streamlined workflow, reducing the required sample volume and preparation time while enhancing assay sensitivity. Furthermore, this study underscores the importance of optimizing the system by considering factors such as autothermal effects, device robustness, sampling volume, aerosolized particle size distribution, and nebulization rate to maximize performance. The studies demonstrate the potential of SAW devices as a promising tool for advancing lipidomics and biological vesicle analysis in biomedical research. Future work will expand on this foundation by exploring the application of SAW devices to EVs such as exosomes, lipid aggregates, and lipid–protein complexes, further broadening the scope and impact of this innovative platform.

Author contributions

Y. H.: drafted the manuscript; developed methods for studying frequency-dependent nebulization and MS analysis; designed, fabricated, and validated SAW devices; setup experiments. Q. M.: optimized experimental methods for MS; revised draft manuscript. A. T.: collected experimental data for SAW nebulization for mass spectrometry. L. L.: collected data for nebulization rate, droplet sizes measurement, and heating experiments. T. E.-N.: guided experimental design for mass spectrometry and liposome studies; revised draft manuscript. V. B.: guided SAW devices design, production and optimization; supervised the project; revised draft manuscript.

Conflicts of interest

There are no conflicts to declare.

Data availability

The data supporting this article, including all mass-spectrometry extracted ion chromatogram results, are provided in the SI. See DOI: **https://doi.org/10.1039/D5LC00692A**.

Acknowledgements

This work is supported by the National Science Foundation, Grant Number: 2108795.

Notes and references

1 F. Szoka Jr and D. Papahadjopoulos, *Annu. Rev. Biophys. Bioeng.*, 1980, **9**, 467–508.
2 T. M. Allen and P. R. Cullis, *Adv. Drug Delivery Rev.*, 2013, **65**, 36–48.
3 A. D. Bangham and R. W. Horne, *Nature*, 1962, **196**, 952–953.
4 Z. Liu, M. Xiong, J. Gong, Y. Zhang, N. Bai, Y. Luo, L. Li, Y. Wei, Y. Liu and X. Tan, *Nat. Commun.*, 2014, **5**, 4280.
5 J. Lou and M. D. Best, *Chem. Phys. Lipids*, 2020, **232**, 104966.
6 A. V. Kabanov, E. V. Batrakova and V. Y. Alakhov, *Adv. Drug Delivery Rev.*, 2002, **54**, 759–779.
7 E. A. Smits, J. A. Soetekouw, I. van Doormalen, B. H. van den Berg, M. P. van der Woude, N. de Wijs-Rot and H. Vromans, *J. Pharm. Biomed. Anal.*, 2015, **115**, 552–561.
8 R. Klein, *Chem. Phys. Lipids*, 1978, **21**, 291–312.
9 K. Gupta, J. Li, I. Liko, J. Gault, C. Bechara, D. Wu, J. T. S. Hopper, K. Giles, J. L. P. Benesch and C. V. Robinson, *Nat. Protoc.*, 2018, **13**, 1106–1120.
10 A. Fauland, H. Köfeler, M. Trötzmüller, A. Knopf, J. Hartler, A. Eberl, C. Chitraju, E. Lankmayr and F. Spener, *J. Lipid Res.*, 2011, **52**, 2314–2322.
11 K. Yang and X. Han, *Metabolites*, 2011, **1**, 21–40.
12 Y. Fan, M. Marioli and K. Zhang, *J. Pharm. Biomed. Anal.*, 2021, **192**, 113642.
13 A. Gomez-Hens and J. Fernandez-Romero, *TrAC, Trends Anal. Chem.*, 2006, **25**, 167–178.
14 R. J. Simpson, J. W. Lim, R. L. Moritz and S. Mathivanan, *Expert Rev. Proteomics*, 2009, **6**, 267–283.
15 M. W. K. Wong, N. Braidy, R. Pickford, P. S. Sachdev and A. Poljak, *Front. Neurol.*, 2019, **10**, 879.
16 N. M. Suni, H. Aalto, T. J. Kauppila, T. Kotiaho and R. Kostiainen, *J. Mass Spectrom.*, 2012, **47**, 611–619.
17 N. E. Manicke, M. Nefliu, C. Wu, J. W. Woods, V. Reiser, R. C. Hendrickson and R. G. Cooks, *Anal. Chem.*, 2009, **81**, 8702–8707.
18 D. Sun, K. F. Böhringer, M. Sorensen, E. Nilsson, J. S. Edgar and D. R. Goodlett, *Lab Chip*, 2020, **20**, 3269–3277.

19 W. J. Perry, N. H. Patterson, B. M. Prentice, E. K. Neumann, R. M. Caprioli and J. M. Spraggins, *J. Mass Spectrom.*, 2020, **55**, e4491.
20 X. Liu, N. Rong, Z. Tian, J. Rich, L. Niu, P. Li, L. Huang, Y. Dong, W. Zhou and P. Zhang, *Sci. Adv.*, 2024, **10**, eadk1855.
21 S. Mahon, *IEEE Trans. Semicond. Manuf.*, 2017, **30**, 494–499.
22 Y. Huang, P. K. Das and V. R. Bhethanabotla, *Sens. Actuators Rep.*, 2021, **3**, 100041.
23 A. N. Taylor, Y. Huang, C. Sircher, S. Khalife, V. Bhethanabotla and T. Evans-Nguyen, *Anal. Chem.*, 2023, **95**, 13497–13502.
24 M. Penza, F. Antolini and M. V. Antisari, *Sens. Actuators, B*, 2004, **100**, 47–59.
25 J. Devkota, P. R. Ohodnicki and D. W. Greve, *Sensors*, 2017, **17**, 801.
26 J. Shi, H. Huang, Z. Stratton, Y. Huang and T. J. Huang, *Lab Chip*, 2009, **9**, 3354–3359.
27 S. K. R. S. Sankaranarayanan, R. Singh and V. R. Bhethanabotla, *J. Appl. Phys.*, 2010, **108**, 104507.
28 W. Sui and P. X.-L. Feng, *Appl. Phys. Lett.*, 2024, **125**(2), 022201.
29 P. K. Das, Y. Huang, T. Evans-Nguyen and V. R. Bhethanabotla, *2022 IEEE Sensors*, 2022, pp. 1–3.
30 Y. Q. Fu, Y. Li, C. Zhao, F. Placido and A. Walton, *Appl. Phys. Lett.*, 2012, **101**, 19.
31 J. Ning, Y. Lei, H. Hu and C. Gai, *Micromachines*, 2023, **14**, 1543.
32 Y. Guo, A. Dennison, Y. Li, J. Luo, X.-T. Zu, C. Mackay, P. Langridge-Smith, A. Walton and Y. Q. Fu, *Microfluid. Nanofluid.*, 2015, **19**, 273–282.
33 S. R. Heron, R. Wilson, S. A. Shaffer, D. R. Goodlett and J. M. Cooper, *Anal. Chem.*, 2010, **82**, 3985–3989.
34 S. H. Yoon, Y. Huang, J. S. Edgar, Y. S. Ting, S. R. Heron, Y. Kao, Y. Li, C. D. Masselon, R. K. Ernst and D. R. Goodlett, *Anal. Chem.*, 2012, **84**, 6530–6537.
35 S. H. Yoon, T. Liang, T. Schneider, B. L. Oyler, C. E. Chandler, R. K. Ernst, G. S. Yen, Y. Huang, E. Nilsson and D. R. Goodlett, *Rapid Commun. Mass Spectrom.*, 2016, **30**, 2555–2560.
36 L. Song, Y. You and T. Evans-Nguyen, *Anal. Chem.*, 2018, **91**, 912–918.
37 S. K. Sankaranarayanan, S. Cular, V. R. Bhethanabotla and B. Joseph, *Phys. Rev. E: Stat., Nonlinear, Soft Matter Phys.*, 2008, **77**, 066308.
38 A. Wixforth, C. Strobl, C. Gauer, A. Toegl, J. Scriba and Z. V. Guttenberg, *Anal. Bioanal. Chem.*, 2004, **379**, 982–991.
39 J. Li, M. H. Biroun, R. Tao, Y. Wang, H. Torun, N. Xu, M. Rahmati, Y. Li, D. Gibson and C. Fu, *J. Phys. D: Appl. Phys.*, 2020, **53**, 355402.
40 L. Y. Yeo, J. R. Friend, M. P. McIntosh, E. N. Meeusen and D. A. Morton, *Expert Opin. Drug Delivery*, 2010, **7**, 663–679.
41 A. Qi, L. Y. Yeo and J. R. Friend, *Phys. Fluids*, 2008, **20**, 7.
42 A. R. Rezk, O. Manor, J. R. Friend and L. Y. Yeo, *Nat. Commun.*, 2012, **3**, 1167.
43 A. Winkler, P. Bergelt, L. Hillemann and S. Menzel, *Open Acoust. J.*, 2016, **6**, 23–33.
44 M. Kurosawa, T. Watanabe, A. Futami and T. Higuchi, *Sens. Actuators, A*, 1995, **50**, 69–74.
45 D. J. Collins, O. Manor, A. Winkler, H. Schmidt, J. R. Friend and L. Y. Yeo, *Phys. Rev. E: Stat., Nonlinear, Soft Matter Phys.*, 2012, **86**, 056312.
46 M. Roudini, D. Niedermeier, F. Stratmann and A. Winkler, *Phys. Rev. Appl.*, 2020, **14**, 014071.
47 S. Kooij, A. Astefanei, G. L. Corthals and D. Bonn, *Sci. Rep.*, 2019, **9**, 6128.
48 S. Xiong, L. Chin, K. Ando, T. Tandiono, A. Liu and C. Ohl, *Lab Chip*, 2015, **15**, 1451–1457.
49 Q.-Y. Huang, Y. Le, H. Hu, Z.-j. Wan, J. Ning and J.-L. Han, *Sci. Rep.*, 2022, **12**, 7930.
50 M. Roudini, J. M. Rosselló, O. Manor, C.-D. Ohl and A. Winkler, *Ultrason. Sonochem.*, 2023, **98**, 106530.
51 W. Akstaller, R. Weigel and A. Hagelauer, *IEEE Trans. Ultrason. Ferroelectr. Freq. Control*, 2020, **67**, 2423–2432.
52 J. Kondoh, N. Shimizu, Y. Matsui and S. Shiokawa, *IEEE Trans. Ultrason. Ferroelectr. Freq. Control*, 2005, **52**, 1881–1883.
53 P. K. Das and V. R. Bhethanabotla, *arXiv*, 2024, preprint, arXiv:2410.18755, DOI: **10.1017/jfm.2025.10179**.
54 P. K. Das, A. D. Snider and V. R. Bhethanabotla, *Phys. Fluids*, 2019, **31**, 10.